Modulation of electronic and transport properties of bilayer heterostructures: InSe/MoS₂ and InSe/h-BN as the prototype

Raja Sen ⬤,* Kasturie Jatkar,† and Priya Johari‡

Department of Physics, School of Natural Sciences, Shiv Nadar University, Greater Noida, Gautam Buddha Nagar, UP 201314, India

Despite having the fascinating physical, electronic, and optical properties of two-dimensional (2D) crystals of MoS₂, h-BN, and InSe, none of them solely meet all the desired criteria required for high efficiency optoelectronic devices, such as a suitable band gap with very high carrier mobility, a moderate excitonic lifetime, a desirable bending modulus, environmental stability against air and water, etc. Herein, we demonstrate that these fundamental limitations can easily be overcome by building a van der Waals heterostructure (vdW-HS) of monolayer InSe either with single-layer MoS₂ or h-BN. Our first-principles calculations suggest that compared to individual monolayers, the examined InSe/MoS₂ and InSe/h-BN vdW-HSs are not only thermodynamically and mechanically more robust but also possess improved electronic and optical properties, which can be particularly useful for solar harvesting devices. Importantly, through a systematic study, we elucidate that the band gap and its nature can largely be modulated ($\sim$0.1–1.6 eV, indirect $\rightleftharpoons$ direct, type I $\rightleftharpoons$ type II) for both the examined heterobilayers by applying mechanical strain and transverse electric field. Even more interestingly, we further show that with such bilayer heterostructures it is possible to get electron and hole mobility almost in the same order of magnitude (10^3–10^4 cm² V⁻¹ s⁻¹), either naturally or by applying small biaxial strain.

I. INTRODUCTION

Since the successful exfoliation of graphene from graphite [1], extensive research efforts have been made to avail the benefits of electronic confinement within graphene for various device applications [2–4]. Besides graphene, a monolayer of hexagonal boron nitride (h-BN) from the graphene family [5] and molybdenum disulfide (MoS₂) belonging to the family of transition-metal dichalcogenides [6] are among the most studied materials of the two-dimensional (2D) family. Although these 2D materials have been widely studied for applications in optoelectronic devices, none of them meet all the essential criteria for modern technology. For example, a reasonable excitonic lifetime [7], a suitable band gap (i.e., closed to the Shockley-Queisser limit of 1.4 eV for the application in photovoltaic devices) [8], high ambipolar charge transport [9], a considerable bending modulus [10], stability against air and water [11], etc., to name a few. Among other potential 2D materials, post-transition-metal chalcogenide-based semiconducting indium selenide (InSe) has recently been explored as a promising 2D material for high-performance electronic and optoelectronic devices [12–14]. Similar to graphene, nanoflakes of InSe can be extracted from the γ-polytype of bulk InSe (space group $R3m$) using mechanical or solvent-based exfoliation methods. Most

interestingly, while graphene-based optoelectronic devices are still on the agenda due to its semimetallic character, the semiconducting InSe monolayer shows promise for device applications due to its tunable band gap and high electron mobility (10^3 cm² V⁻¹ s⁻¹) at room temperature [14,15]. In addition, its 2D density of states gives rise to a one-dimensional "Van Hove singularity," which is fundamentally responsible for tunable magnetism, superconductivity, and enhanced thermoelectricity [12,16]. However, despite having several fascinating physical properties, few-layer InSe-based electronic devices have been seen to face a long-term stability issue, primarily due to their intrinsic Se vacancy [17,18]. Thus, special care, such as surface passivation with other layers (e.g., boron-nitride, graphene, or In-based oxide layers) [14,18,19] or Se vacancy filling through thiol treatment [17], is quite necessary to enhance the stability of InSe-based devices. Simultaneously, various other drawbacks of monolayer InSe, such as low optical response near the band edge [14], low hole mobility [20,21], etc., remain to be solved before its practical application in optoelectronic devices in general, and ambipolar field-effect transistors and photovoltaics in particular.

As mentioned above, these 2D materials (InSe, MoS₂, and h-BN) lack one or more features that are required for multifunctional high-performance device applications. In this regard, bilayer heterostructures of these materials can prove helpful in concealing their deficiencies by complementing each other's favorable characteristics. Just as in graphene/MoS₂ van der Waals heterostructure (vdW-HS), the issues of zero band gap in graphene and low electron mobility in MoS₂ have been covered up by the band gap of MoS₂ and high electron mobility of graphene, respectively. However,

*rs190@snu.edu.in
†Present address: Department of Physics and Astronomy, Uppsala University, Sweden.
‡Corresponding author: priya.johari@snu.edu.in, psony11@gmail.com

they could not match each other's strengths up to the mark. The band could not open up to the band gap of MoS_2, nor could the electron mobility reach the value of graphene's mobility [22,23]. With an aim to adopt the best of the properties and curtail the unwanted issues, we studied $InSe/MoS_2$ and $InSe/h$-BN bilayer heterostructures as the prototype, using first-principles density functional theory (DFT) [24]. Our study found that these heterostructures overcome individual flaws by relying on each other's strengths.

We also examined the scope for tuning the properties of these heterostructures. For this purpose, we applied mechanical strain and an external electric field to tune the electronic and transport properties of these two bilayer heterostructures. However, it is also noteworthy that Chen *et al.* [25] and Zhang *et al.* [26] have recently studied the $InSe/MoS_2$ HS using first-principles calculations. Their study established that such a 2D bilayer holds promise for optoelectronic devices with a tunable band gap and optical absorption over a wide range of the solar spectrum (300–800 nm). But, their study is limited to this extent only and does not examine the mechanical and charge transport properties of $InSe/MoS_2$ vdW-HS, which are crucial for their application in optoelectronic devices in general, and photovoltaics in particular. Moreover, their HS exhibits an in-built strain of over 2%, which can dramatically alter the electronic properties of a monolayer of both InSe [27] as well as MoS_2 [28,29]. Thus, to accurately predict the variation in the properties of InSe due to its hybridization with MoS_2 or h-BN, we have minimized the strain on the component layers to $\leqslant 1\%$ while modeling the $InSe/MoS_2$ and $InSe/h$-BN HSs.

At the DFT level of theory, both of our examined vdW-HSs are found to be semiconductors with an indirect band gap. However, it has also been shown that both the band gap and its nature for the examined vdW-HSs can largely be tuned under mechanical strain and transverse electric field. A detailed investigation of optical properties demonstrates the enhancement of the light absorption capabilities in these vdW-HSs compared to their constituent layers. With regard to transport properties, it has been shown that electron mobility can be improved in both vdW-HSs as compared to monolayer InSe. Furthermore, the limitation of hole mobility of monolayer InSe is demonstrated to be overcome with $InSe/MoS_2$ vdW-HS, which is found to exhibit ambipolar charge transport characteristic at room temperature with high electron and hole mobility. Concurrently, $InSe/h$-BN vdW-HS has also been found to possess an ambipolar charge transport characteristic at room temperature under small biaxial mechanical strain. Furthermore, our study also demonstrates that compared to individual monolayers, the mechanical properties of 2D materials, such as Young and bending modulus, can be dramatically improved in the examined heterobilayers, making them a potential candidate for flexible optoelectronic devices. We systematically present all our results in the following sections with a proper understanding of the underlying physics.

II. METHODS

Ab initio structure relaxations and electronic structure calculations were carried out using the Vienna Ab-initio Simulation Package (VASP) [30,31], within the framework of DFT [24]. The calculational details of all the investigated properties of the considered monolayers and their vdW-HSs are described in the Supplemental Material [32] (see, also, Refs. [33–56] therein).

III. RESULTS AND DISCUSSIONS

In the following sections, we present our results addressing the structural, electronic, optical, elastic, and transport properties of $InSe/MoS_2$ and $InSe/h$-BN vdW-HSs. The effect of applied strain and induced electric field on the electronic and transport properties of these vdW-HSs is also systematically investigated, and the corresponding results are compared with that of the respective unperturbed system.

A. Structures and stability

To analyze the structural changes within both of the monolayers due to vdW stacking in $InSe/MoS_2$ and $InSe/h$-BN, we studied the structural properties of the individual monolayers as well as their heterobilayers. A schematic illustration of the optimized structures of monolayer InSe, MoS_2, and h-BN is presented in Fig. 1. All these monolayers exhibit hexagonal lattice symmetry in the xy-plane. The lattice constants of InSe, MoS_2, and h-BN are calculated to be 4.12, 3.18, and 2.47 Å, respectively, while the thickness of InSe and MoS_2 is estimated to be $d_{Se-Se} = 5.40$ Å and $d_{S-S} = 3.13$ Å, respectively, which agree well with the previous results [29,37–40].

To minimize the lattice mismatch between the monolayers in the examined vdW-HSs, we model $InSe/MoS_2$ with a $2\sqrt{3} \times 2\sqrt{3}R30^{\circ}$ supercell of MoS_2 (11.02 Å) monolayer on top of a $\sqrt{7} \times \sqrt{7}R19.11^{\circ}$ supercell of InSe (10.90 Å) monolayer, while our $InSe/h$-BN comprises the stacking of 5×5 and 3×3 supercells of h-BN (12.35 Å) and InSe (12.36 Å) monolayers, respectively, as depicted in Fig. 1. On relaxing these HSs, the optimized lattice constants of $InSe/MoS_2$ and $InSe/h$-BN are calculated to be 11.02 and 12.56 Å, respectively. Thus, the lattice constant of $InSe/MoS_2$ remained primarily of the supercell of MoS_2 (11.02 Å), while in the case of $InSe/h$-BN the optimized lattice (12.56 Å) is found to be $\sim$1.6% larger than their constituent supercells (see Tables S1 and S2 of the Supplemental Material [32]). The optimized interlayer distance in $InSe/MoS_2$ is estimated to be 3.46 Å compared with interlayer distances of 3.37 and 3.07 Å in pristine InSe and MoS_2, respectively, in agreement with the recent work of Zhang *et al.* [26], while it is predicted to be 3.52 Å for $InSe/h$-BN vdW-HS (interlayer distance in pristine h-BN is 3.30 Å). It is also noted here that after construction of these vdW-HSs, atomic bond lengths remained unaltered, while a minute change was noticed in the thickness and buckling height of the InSe layer (see Table S2 of the Supplemental Material [32]). On moving from an isolated layer of InSe to $InSe/MoS_2$ and $InSe/h$-BN, the thickness (d_{Se-Se}) of the InSe layer was found to decrease from 5.40 Å to 5.34 and 5.33 Å and the buckling height from 1.28 Å to 1.25 and 1.24 Å, respectively.

To check the relative stability of $InSe/MoS_2$ and $InSe/h$-BN so that they can be realized experimentally, we first calculate the binding energies of the examined HSs with
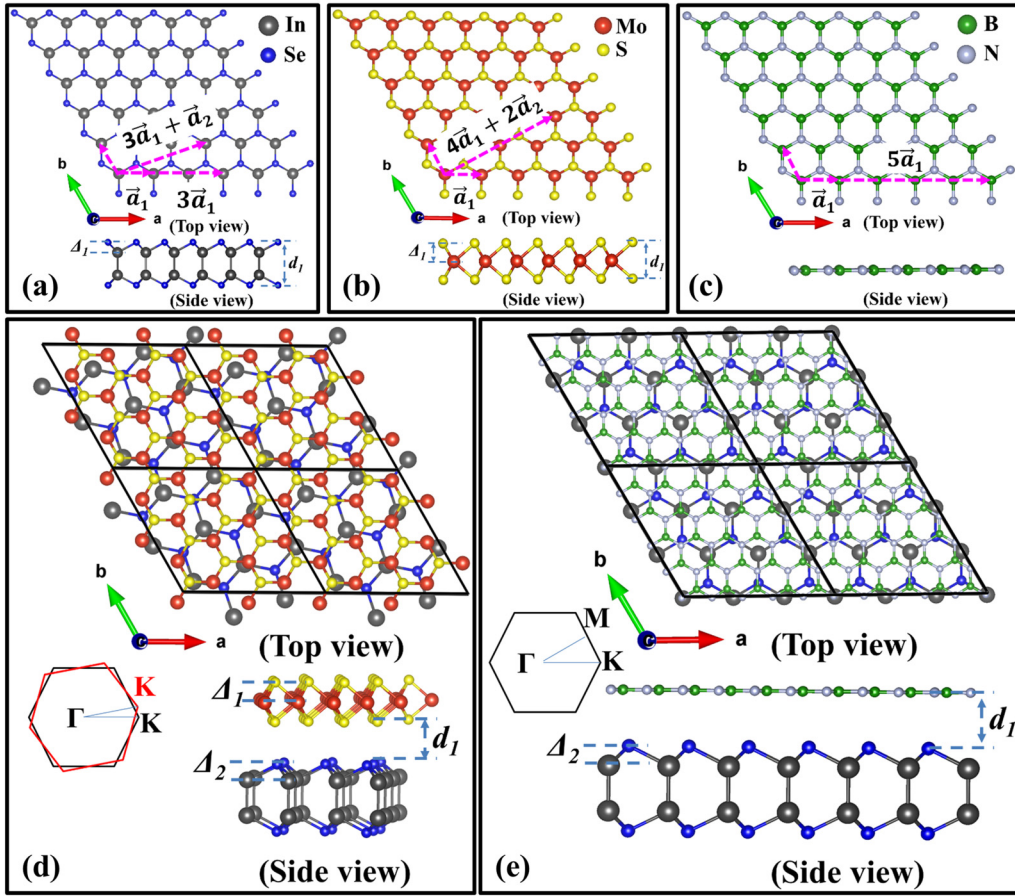
FIG. 1. A schematic ball-and-stick representation of the optimized structures of monolayer (a) InSe, (b) MoS_2, and (c) h-BN; and the examined (d) $InSe/MoS_2$ and (e) $InSe/h$-BN vdW-HSs. In each part, the top and bottom panels correspond to the top and side view of the structures. Pink dotted lines in (a)–(c) represent the supercell basis vectors of each constituent layer considered in building the $InSe/MoS_2$ and $InSe/h$-BN vdW-HSs, while the corresponding data are presented in Table S1 of the Supplemental Material [32]. The interlayer distance (d_1), buckling hight (Δ_1 and Δ_2 for InSe and MoS_2 layers, respectively), and the overlap of the primitive-cell Brillouin zones of each monolayer in the constructed heterobilayer are also illustrated with their respective vdW-HSs, and the corresponding data are tabulated in Table S2 of the Supplemental Material [32].

respect to the total energy of the component monolayers using the following equation:

$$E_b = \left(E_{\text{vdW-HS}} - \sum_i E_{\text{monolayer}_i} \right) \Big/ A, \qquad (1)$$

where $E_{\text{vdW-HS}}$ and $E_{\text{monolayer}_i}$ are the total energies of vdW-HS and that of the isolated component layers, respectively, and A is the optimized interfacial area.

Our calculations confirm the examined vdW-HSs to be energetically stable with binding energies of -16.67 and -15.91 meV/Å^2 for $InSe/MoS_2$ and $InSe/h$-BN, respectively. Interestingly, these binding energies are much lower than the binding energy of the recently investigated InSe-phosphorene heterostructure (-9.03 meV/Å^2) [63]. However, to confirm the thermodynamical stability of any material, it is essential to check their dynamical and mechanical stability as well. But, due to the large supercell and the large number of atoms per unit cell (64 and 86 atoms per unit cell in $InSe/MoS_2$ and $InSe/h$-BN, respectively), it is not computationally feasible to examine their dynamical stability through phonon dispersion curves. Therefore, here we focus only on examining the

mechanical stability of the vdW-HSs. The in-plane elastic stiffness constants (C_{ij}) of the investigated vdW-HSs are depicted in Table I, while detailed mechanical properties of the investigated structures are discussed in Sec. III E. It should be mentioned here that the elastic coefficient C_{11} measures the tensile or compression stiffness of 2D crystal parallel to the crystallographic a-axis, C_{12} represents the ability of 2D materials to resist biaxial strain, while C_{66} is correlated with the in-plane shear strain of 2D crystal [64,65]. Due to the hexagonal symmetry, C_{11} and C_{12} are independent of each other here, while $C_{22} = C_{11}$ and $C_{66} = (C_{11} - C_{12})/2$ [57]. On analyzing the C_{ij} values, we found that all elastic constants are greater than zero and they also satisfy Born's criterion for mechanical stability, i.e., $C_{11} - C_{12} > 0$. This analysis thus elucidates that both of the vdW-HSs hold promise to be realized in practice.

B. Electronic properties

An in-depth knowledge of electronic structures, particularly for any low-dimensional material, is highly crucial for their application in optoelectronic devices. Analyzing

TABLE I. Elastic properties of InSe/MoS$_2$ and InSe/h-BN heterobilayers, presented with their component monolayers. The elastic constants (C_{ij}), shear modulus (G), layer modulus (γ), and Young's modulus (Y) are in N m^{-1}, the bending modulus (D) is in eV, while Poisson's ratio (ν) is a dimensionless quantity. Data from other studies are also given for comparison.

System	C_{11}	C_{12}	$C_{66} = G_{2D}$	γ	Y	ν	D	Reference
InSe/MoS$_2$	145.13	23.27	60.93	84.20	141.40	0.16	107.98	This work
InSe/h-BN	324.18	58.01	133.08	191.09	313.80	0.18	155.39	This work
InSe	47.98	11.92	18.03	29.95	45.02	0.25	7.28	This work
					45.61	0.28		Ref. [27] (Theory)
MoS$_2$	130.16	30.61	49.78	80.38	122.96	0.23	6.63	This work
	132.3	32.8	49.5	82.5	124.1	0.25		Ref. [57] (Theory)
							9.61	Ref. [58] (Theory)
					123	0.25		Ref. [59] (Expt.)
h-BN	315.70	79.99	117.85	197.84	295.43	0.25	0.92	This work
	293.20	66.10			278.30			Ref. [60] (Theory)
							0.95	Ref. [61] (Theory)
					288.91[a]			Ref. [62] (Expt.)

[a]Considering the effective thickness of single-layer BN to be 0.334 nm from Ref. [62].

the electronic structures of the component layers, we found that under the opt-PBE (optimized-Perdew-Burke-Ernzerhof) functional our calculations estimate the band gap of monolayer InSe, MoS$_2$, and h-BN to be 1.24 (indirect: $\Gamma - M \to \Gamma$), 1.68 (direct: $K \to K$), and 4.05 eV (indirect: $K \to \Gamma$), respectively [see Figs. S1 (a)–(c) of the Supplemental Material [32]], in agreement with previous theoretical results [29,37–40]. However, it is well known that the PBE functional in general underestimates the experimental band gap for monolayers. We also noticed the same thing as the experimental band gaps of a monolayer of InSe, MoS$_2$, and h-BN are reported as 2.91 [14], 1.80 [66,67], and 6.10 eV [68], respectively. Therefore, for a proper description of electronic structures, calculations using a hybrid functional, such as HSE06 (Heyd-Scuseria-Ernzerhof) or quasiparticle (QP)-based GW (G and W represent the Green's function and screened interaction, respectively) calculations, are generally preferred. On considering the HSE06+D3 functional, we calculate the band gap to be 1.90 eV for InSe and 5.21 eV for h-BN monolayer [see Figs. S1 (d) and (f) of the Supplemental Material [32]], respectively. These values match well with the previous theoretical calculations [14,37,40,69,70] and have been found to show a better agreement with the experimental value as we moved from the PBE to the HSE06 method. In contrast, in the case of MoS$_2$ monolayer, it overestimates the experimental band gap by 0.52 eV, giving a value of 2.32 eV [see Fig. S1 (e) of the Supplemental Material [32]], in agreement with previous calculations [28,67]. The GW-based quasiparticle band-structure calculations may give a proper description of the InSe band structure [37], but they are known to highly overestimate the band gap of monolayer MoS$_2$ and h-BN [40,67,71]. In addition to this, such calculations are extremely expensive as well, and for the kind of vdW-HSs (having large unit cell) considered in this work they are beyond the scope. It should also be noted that spin-orbit coupling (SOC) has also been found to have a little effect on the electronic structures of these monolayers [26,72]. For monolayer InSe and MoS$_2$, the band gap increases by 0.03 [25] and 0.07 eV [73] on considering SOC in calculations, while SOC is found to have almost no effect on the band gap of monolayer h-BN [73]. Therefore, to be cost-effective yet having a reasonable

qualitative estimation, we primarily considered the opt-PBE functional (without SOC) to analyze electronic structures of InSe/MoS$_2$ and InSe/h-BN heterostructures and their modulation under strain and induced electric field. However, for reference we also provide the HSE06+D3 band structures for two of our examined vdW-HSs in Fig. S2 of the Supplemental Material [32].

Under consideration of opt-PBE and HSE06+D3 functionals, our electronic structure calculations reveal that both of the examined vdW-HSs are indirect band-gap semiconductors. The opt-PBE functional calculates a band gap of $\sim$1 eV for both HSs [see Figs. 2(a) and 2(c)], while the HSE06 functional estimates the band gaps of InSe/MoS$_2$ and InSe/h-BN to be
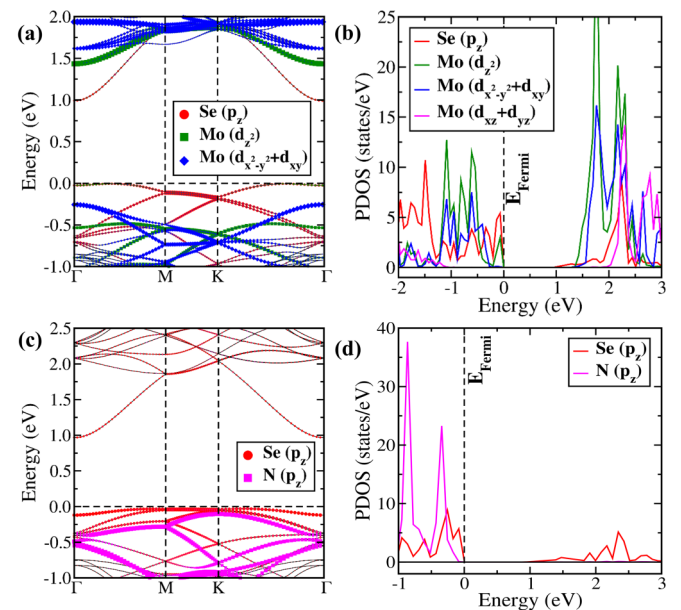
FIG. 2. Electronic band structures and partial density of states (PDOS) of (a) and (b) InSe/MoS$_2$ and (c) and (d) InSe/h-BN vdW-HSs calculated using the opt-PBE functional, respectively. Here, the Fermi level is set at 0 eV and shown by horizontal (vertical) black dashed lines in their respective band (PDOS) structures.

1.61 and 1.71 eV [see Figs. S2 (a) and (b) of the Supplemental Material [32]], respectively. Thus, both functionals predict a considerably lower band gap for the HSs as compared to the respective band gap of the constituent layers. Our predicted band gap for InSe/MoS$_2$ also agrees well with the recent work of Chen *et al.* [25]. In both systems, the conduction-band minimum (CBM) is found to be located at the Γ point of the Brillouin zone. The valence-band maximum (VBM), however, is found to lie near the Γ point along the Γ-*M* line in the case of InSe/MoS$_2$ and toward the *M* point along the Γ-*M* line in InSe/*h*-BN. In InSe/*h*-BN, both VBM and CBM arise due to the Se-p_z orbital, whereas in InSe/MoS$_2$, both Mo-d_{z^2} and Se-p_z orbitals contribute to the VBM, while the Se-p_z orbital dictates the CBM [see Figs. 2(a)–2(d)]. This suggests that InSe/*h*-BN has a type I band alignment, while InSe/MoS$_2$ appears to exhibit an intermediate band alignment between type I and type II. To qualitatively understand this behavior, we plotted the band alignment (with respect to the vacuum energy level) of the isolated monolayers within the same cell geometry as considered into the heterostructures in Fig. S3 of the Supplemental Material [32]. It can be seen that in InSe/*h*-BN, the VBM (CBM) of InSe (3 × 3 supercell) and *h*-BN (5 × 5 supercell) lies at −6.50 eV (−5.49 eV) and −7.91 eV (−3.77 eV), respectively. Thus, in this case the VBM and CBM of InSe monolayer are closest to the Fermi level of InSe/*h*-BN vdW-HS (−5.44 eV), and hence they contribute to forming the VBM and CBM of InSe/*h*-BN. The VBM and CBM of InSe monolayer ($\sqrt{7} \times \sqrt{7}R19.11^\circ$) are also found nearest to the Fermi level (−5.54 eV) of InSe/MoS$_2$ vdW-HS with band offset $\Delta_{VB} = E_{VBM}^{InSe} - E_{VBM}^{MoS^2} = 0.33$ eV and $\Delta_{CB} = E_{CBM}^{InSe} - E_{CBM}^{MoS^2} = -0.29$ eV, but unlike InSe/*h*-BN, an interlayer hybridization occurred in between Mo-d_{z^2} and Se-p_z orbitals [see Figs. 2(a) and 2(b)] due to close packing of the monolayers and the vdW interactions between them, which results in a new electronic state at the VBM of InSe/MoS$_2$.

To gain further insight into the interlayer interactions and the charge-transfer mechanism between the two monolayers in the constructed heterostructures, we calculate the charge-density difference (CDD) as follows:

$$\Delta\rho = \rho_{InSe/X} - \rho_{InSe} - \rho_X,$$

where X represents MoS$_2$ or *h*-BN monolayer, and $\rho_{InSe/X}$, ρ_{InSe}, and ρ_X are the charge density of the examined vdW-HS, the isolated InSe monolayer, and the isolated X monolayer, respectively. To visualize the CDDs, we present their isosurfaces in Fig. 3, together with the plane-averaged CDD along the z direction, where yellow (cyan) denotes a depletion (accumulation) of electrons. It can be seen from Fig. 3 that charges are mainly redistributed in the interface region, forming a series of surface dipoles. However, a noticeable difference is observed in their distribution on going from InSe/*h*-BN to InSe/MoS$_2$. In InSe/*h*-BN, electrons are mainly accumulated near the *h*-BN site and depleted from the InSe layer [see Figs. 3(c) and 3(d)], while in the case of InSe/MoS$_2$ an electron cloud is mainly found in the middle of two layers [see Figs. 3(a) and 3(b)]. It occurs primarily due to the comparatively large electronegativity difference between Se
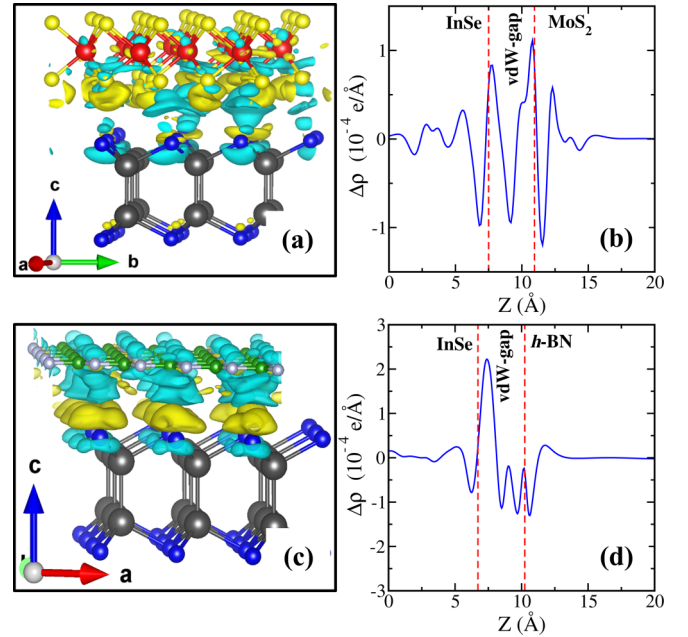
FIG. 3. The schematic view of the charge-density difference of (a) InSe/MoS$_2$ and (c) InSe/*h*-BN-based vdW-HSs. The cyan and yellow isosurfaces correspond to the accumulation and depletion of electrons (Isovalue 10^{-4} $e\text{Å}^{-3}$). The plane-averaged charge-density difference plots of (b) InSe/MoS$_2$ and (d) InSe/*h*-BN based vdW-HSs are also presented for reference, where −ve and +ve values of $\Delta\rho$ represents the accumulation and depletion of electrons, respectively.

and N atoms in InSe/*h*-BN compared with that between Se and S atoms in InSe/MoS$_2$ vdW-HS.

C. Band-gap modulation under strain and electric field

To explore the effect of mechanical strain on the electronic properties of InSe/MoS$_2$ and InSe/*h*-BN vdW-HSs, an in-plane biaxial strain ($\sigma = \Delta a/a_0$, where a_0 is the equilibrium in-plane lattice constant of the considered HSs and Δa is the measure of the lattice dilation) up to ±6% is considered on each of our examined heterobilayers. Since this strain range is close to the elastic regime of the constituent layers [27,60,61,74,75], no out-of-plane buckling is seen to occur within the constituent monolayers in the designed HSs. However, a change in the atomic bond lengths as well as the thickness of the constituent monolayers is noticed in the strained HSs. We found that the thickness of InSe and MoS$_2$ layers in the designed InSe/MoS$_2$ HSs decreases (increases) from 5.34 to 5.10 (5.61) Å and 3.16 to 3.04 (3.31) Å at 6% tensile (compressive) strain, respectively. The In-In, In-Se, and Mo-S bond length in InSe/MoS$_2$ HSs changes from 2.84, 2.71, and 2.42 Å to 2.86 (2.82), 2.78 (2.65), and 2.47 (2.39) Å under 6% tensile (compressive) strain. On the other hand, the thickness of the InSe layer in the designed InSe/*h*-BN HSs is seen to decrease (increase) from 5.33 to 5.07 (5.64) Å at 6% tensile (compressive) strain, while the In-In, In-Se, and B-N distance is calculated as 2.86 (2.83), 2.79 (2.65), and 1.54 (1.40) Å at 6% tensile (compressive) strained structure, respectively. Variation in the band gap with respect to strain
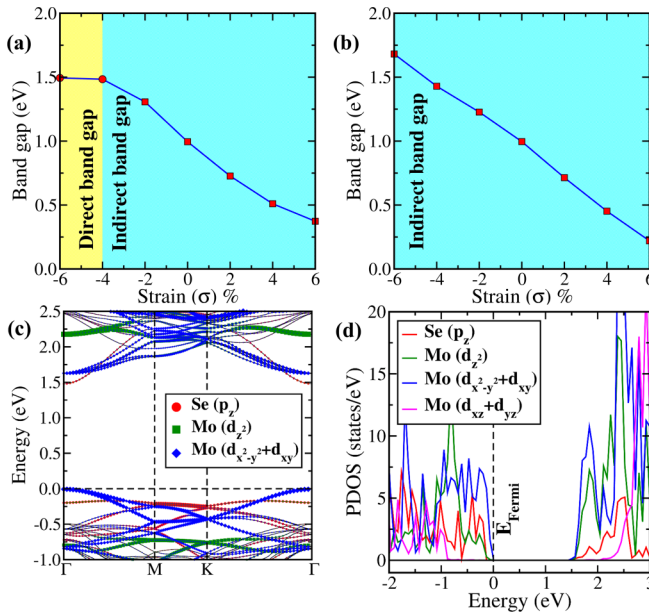
FIG. 4. The variation of the electronic band gap of (a) InSe/MoS$_2$ and (b) InSe/h-BN with mechanical strain, calculated using the opt-PBE functional. In all the figures, the square box (circle) represents the indirect (direct) nature of the band gap. Parts (c) and (d) represent the band structure and partial density of states (PDOS) of InSe/MoS$_2$ vdW-HS at 4% of compressive strain, calculated using the opt-PBE functional. Here, the Fermi level is set at 0 eV and shown by horizontal (vertical) black dashed lines in the respective band (PDOS) structure.

(up to $\sigma = \pm 6\%$) is presented in Figs. 4(a) and 4(b). In the case of InSe/MoS$_2$, on applying tensile strain (i.e., $\sigma > 0$) the band gap is found to decrease monotonically (decreased by ~62.5% at $\sigma = +6\%$ with respect to the unperturbed system) and remain indirect, whereas for compressive strain the band gap attains a maximum value of 1.49 eV at $\sigma = -4\%$ (i.e., increased by ~50.1% at $\sigma = -4\%$ with respect to the unperturbed system) and shows an indirect to direct band gap. To understand the physical reason behind this transition, we compared the band structure of unperturbed InSe/MoS$_2$ HS with the one with $\sigma = -4\%$ [see Figs. 4(c) and 4(d)]. Interestingly, it is found that with compressive strain the hybridized Mo-d_{z^2} and Se-p_z orbitals, which primarily contributed to making the VBM of unstrained InSe/MoS$_2$ HS, have been shifted down, while Mo-$d_{x^2-y^2} + d_{xy}$ energy levels are shifted up to form the VBM of the strained system ($\sigma = -4\%$) at the Γ point. To shed further light, we plot energy levels of the strained InSe/MoS$_2$ HS ($\sigma = -4\%$) with respect to the same strained component layers considered into vdW-HS (see Fig. S4 of the Supplemental Material [32]). Due to strain, the VBM (CBM) of InSe and MoS$_2$ are found to shift at -6.97 eV (-5.25 eV) and -6.62 eV (-4.99 eV), respectively. Thus, contrary to the unstrained InSe/MoS$_2$, the VBM from the MoS$_2$ layer and the CBM from the InSe layer lie closest to the Fermi level (-5.60 eV) of compressively strained InSe/MoS$_2$ HS ($\sigma = -4\%$). As a result, on the application of compressive strain ($\sigma \geqslant -4\%$) InSe/MoS$_2$ attains a direct band gap and becomes a type II band alignment semiconductor. In such systems, photogenerated electron-hole pairs can be spatially

separated with electrons and holes preferably at the InSe and MoS$_2$ layers, respectively, which as a consequence reduce the recombination rate of the electron-hole pairs and enhance their diffusion length. However, it is noteworthy here to mention that a type I to type II band transition in InSe/MoS$_2$ HS could also be obtained via controlling the interlayer distance between the constituent layers. However, Chen *et al.* [25] showed in their study that the change in interlayer distance only affects the nature of the band alignment of InSe/MoS$_2$ HS, but seldom changes the band gap. In the case of InSe/h-BN, no such reordering of energy levels under strain is observed. Thus, similar to the unstrained system, the band gap remains indirect also under the applied strain, and the VBM and CBM are contributed to by the InSe monolayer. The band gap, however, is found to decrease (increase) monotonically with tensile (compressive) strain [see Fig. 4(b)], as also generally observed with monolayer InSe [27]. Our calculations predict an increase (a decrease) in the band gap by ~78% (69%) under tensile (compressive) strain of 6% with respect to the undeformed system. Thus, our study suggests that the band gap of the examined HSs can be widely tuned and its nature can be varied on the application of mechanical strain.

Similar to band modulation of 2D monolayer crystals through strain engineering, an external transverse electric field can also be effective in tuning the band gap and controlling the performance of 2D material based electronic devices via the gate voltage. In the present work, therefore, we also investigate the effect of an external electric field on the electronic properties of InSe/MoS$_2$ and InSe/h-BN HSs. On analyzing the results [see the black curve depicted in Figs. 5(a) and 5(d)], it is found that on changing the electric field from -0.1 to 0.1 V/Å, which is a crucial range for this purpose, the band gap varies marginally by 0.02–0.06 eV, however a relatively larger variation in the band gap is observed beyond $E = \pm 0.1$ V/Å. With positive field, the band gap increases in the case of InSe/MoS$_2$ (up to $E = 0.3$ V/Å), though it remains constant for InSe/h-BN HS. But, upon applying reverse bias [negative electric field (E)], the band gap decreases by 0.21 eV (0.55 eV) in InSe/MoS$_2$ (InSe/h-BN) when the electric field varies from $E = -0.1$ to -0.5 V/Å. Thus, contrary to the strain, with the application of an electric field the electronic properties of the examined HSs can be finely tuned and can be varied by 5–24% (1–60%) in InSe/MoS$_2$ (InSe/h-BN) HS with respect to the unperturbed system. However, throughout the range of electric bias, the nature of the band gap of the examined HSs retains its original character, i.e., an indirect band gap for both the HSs with a type I band alignment for InSe/h-BN HS and an intermediate band alignment between type I and type II for InSe/MoS$_2$ HS. Such band-gap variation against an external electric field is commonly seen in monolayer InSe under an applied electric field [76], and thus it is noticed in the examined HSs as well since the VBM and CBM in our unstrained HSs originate mainly from the InSe monolayer. However, in a recent study Chen *et al.* [25] reported that a type I (indirect) to type II (indirect) band transition can be obtained even by applying the external field to the unstrained InSe/MoS$_2$ HS. Such a discrepancy with our results can be attributed to the way they constructed the HS. In the case of InSe/MoS$_2$ structure, we tried to decrease the lattice mismatch between constituent
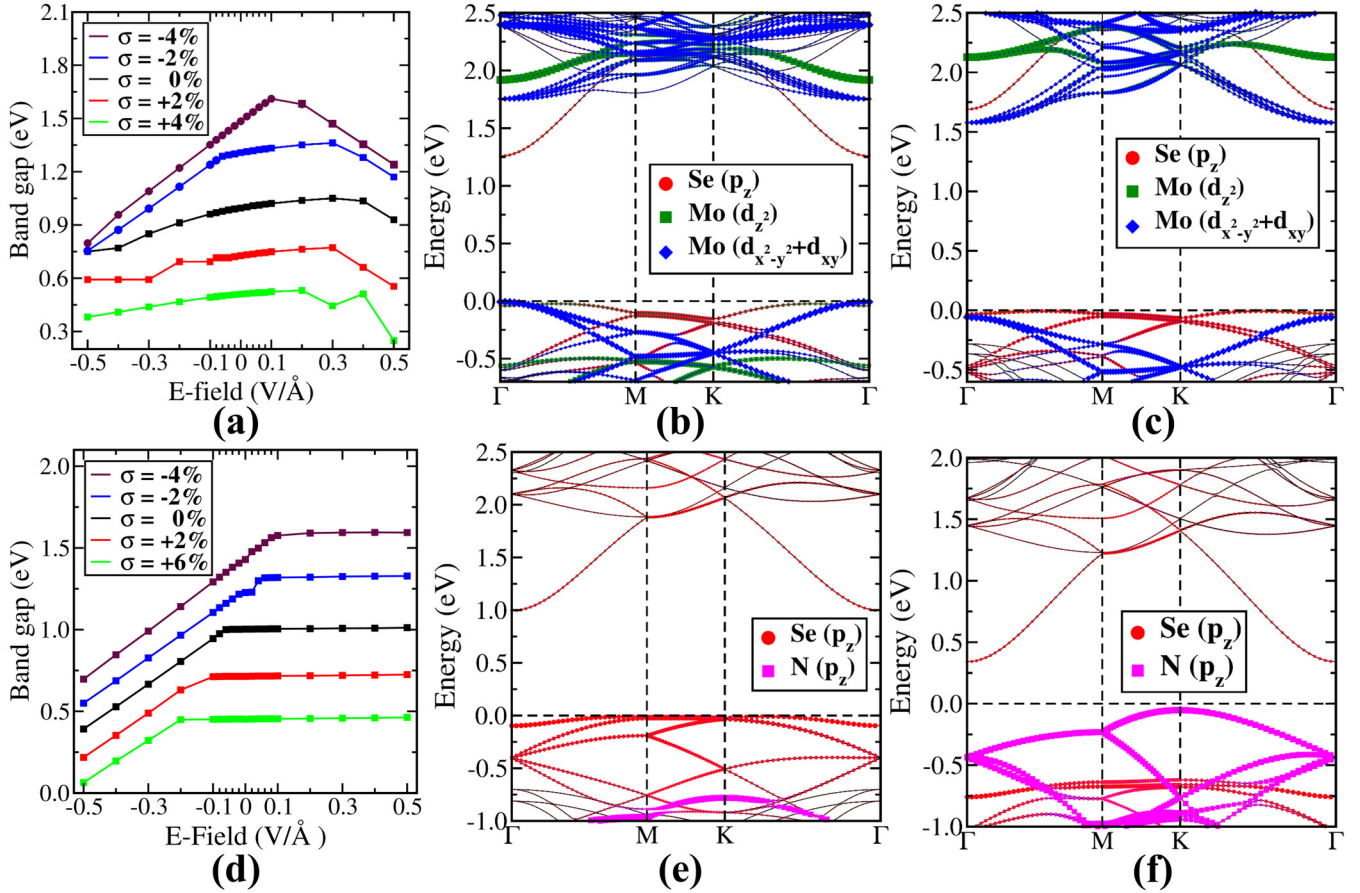
FIG. 5. Change in the band gap of strained and unstrained (a) InSe/MoS$_2$ and (d) InSe/h-BN HSs on the application of transverse electric field is shown. In all figures the square box (circle) represents the indirect (direct) nature of the band gap. Electronic band structures of (b) InSe/MoS$_2$ at $\sigma = -2\%$ and $E = -0.08$ V/Å, (c) InSe/MoS$_2$ at $\sigma = -4\%$ and $E = +0.2$ V/Å, (e) InSe/h-BN at $\sigma = 0\%$ and $E = +0.5$ V/Å, and (f) InSe/h-BN at $\sigma = 0\%$ and $E = -0.5$ V/Å are also presented. Here, the Fermi level is set at 0 eV and shown by a horizontal black dashed line.

layers to ∼1%, while the designed structure of Chen *et al.* includes a strain of ∼2% between the constituent layers. Thus, their results naturally include some effect of external stain on the constituent layers, besides the applied external electric field, and since the electronic properties are quite sensitive to the mechanical strain [27–29], even a small strain in the monolayers has dramatically changed their results. Below, we also demonstrate and discuss that on a strained InSe/MoS$_2$ structure it is possible to get a type I to type II transition by applying the external electric field.

Finally, in order to understand the effect of both strain and electric field on the electronic properties of InSe/MoS$_2$ and InSe/h-BN, the band structure of the strained heterobilayers with $\sigma = \pm2\%$ and $\pm4\%$ is also investigated under a transverse external electrical field varying from $0 - \pm5$ V/Å [see Figs. 5(a) and 5(d)]. Our calculations reveal that on applying the electric field to the strained InSe/MoS$_2$ and InSe/h-BN, the variation in the band gap follows the same trend as observed for the case of an unstrained system under an external electric field. However, in the case of InSe/MoS$_2$ a significant difference is noticed in the nature of the band gap at 2% and 4% compressive strain. At $\sigma = -2\%$, an indirect to direct band gap crossover is found with the increase of negative electric bias, while an increase of positive electric field

leads to a direct to indirect band-gap transition in InSe/MoS$_2$ HS at 4% compressive strain. To gain deep insight into the band transition, we further investigate the electronic structures of the strain-induced InSe/MoS$_2$ HSs against the electric field, mainly where the transition occurs, i.e., at −0.08 and +0.2 V/Å for 2% and 4% of compressive strain, respectively [see Figs. 5(b) and 5(c)]. At 2% of compressive strained structure, the CBM of InSe/MoS$_2$, which originates mainly from Se-p_z orbitals of InSe monolayer, is found to shift downward with the increase of negative electric field, which results in a decrease of the band gap. Concurrently, a crossover between the Mo-$d_{x^2-y^2} + d_{xy}$ state and the hybridized Mo-d_{z^2} and Se-p_z states is also seen near the Fermi level of the valence-band state. Thus, similar to $\sigma \geqslant -4\%$ strained structure, the VBM now originates due to Mo-$d_{x^2-y^2} + d_{xy}$ orbitals, and as a consequence the electronic gap becomes direct, whereas with an increase of a positive electric field in 4% of the compressive strained structure, a similar crossover between the Mo-$d_{x^2-y^2} + d_{xy}$ state and the Se-p_z state is observed in both the valence- and conduction-band states near the Fermi level. As a result, the VBM and CBM of InSe/MoS$_2$ at 4% compressive strain and +0.2 V/Å electric field form by Se-p_z (with little contribution of Mo-d_{z^2} due to interlayer hybridization) and Mo-$d_{x^2-y^2} + d_{xy}$ states, respectively, and
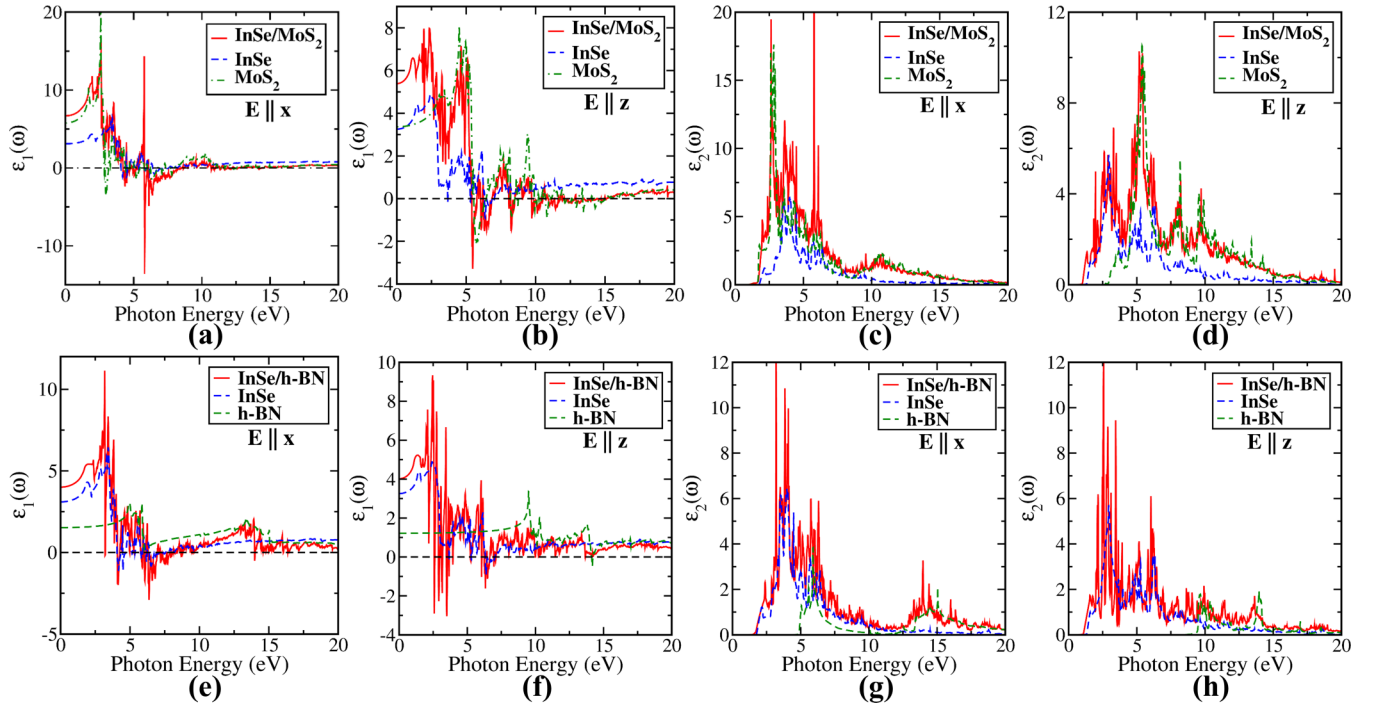
FIG. 6. The real [$\varepsilon_1(\omega)$] and imaginary [$\varepsilon_2(\omega)$] part of the frequency-dependent dielectric function of (a)–(d) InSe/MoS$_2$ and (e)–(h) InSe/h-BN-based vdW-HSs, calculated using the DFT + IPA approach via the opt-PBE functional, along both x and z directions of polarization, respectively.

the corresponding system appears as an indirect band-gap semiconductor under a type II band alignment category. Note that such a transition between atomic orbitals near the VBM is also noticed in the study of Chen *et al.* [25].

In the case of InSe/h-BN we analyze the band structure at two extreme conditions of an external electric field in our case [see Figs. 5(e) and 5(f)]. As expected with monolayer InSe [76], the CBM of InSe/h-BN that comes from the Se-p_z energy level shifts down by only a few meV at +0.5 V/Å of the electric field, and therefore the band gap remains almost constant. However, at $E = -0.5$ V/Å, the VBM of InSe/h-BN is found to shift more along with a crossover between Se-p_z and N-p_z states near the Fermi level of VBM. As a result of the negative electric field, the InSe/h-BN is found to transform from type I band alignment to type II band alignment, although the nature of the band gap remains indirect in all the stages.

D. Optical properties

To understand the light-harvesting capabilities of both the examined HSs, we next investigate their linear optical properties, such as the real (ϵ_1) and imaginary (ϵ_2) part of the frequency-dependent dielectric constant, the absorption coefficient, and the electron energy loss spectrum (EELS), together with their constituent monolayers. These optical features are calculated using the independent particle approximation (IPA) method via state-of-the-art DFT calculations in conjunction with the opt-PBE functional [53,54]. Here, it must be mentioned that the IPA method is generally known not to take into account electron-hole interactions in the excitation process, and therefore it shows some abnormal

dispersion in the optical spectra with an under- or overestimation of peak positions and a drastic fall in the peak intensity along with photon energies, as compared to the *GW* and Bethe-Salpeter equation (BSE) - based results [77–79]. Nevertheless, under a proper choice of exchange-correlation functional, the IPA approach could be an effective way for a qualitative estimation of the peak maxima corresponding to various optical features and their modulation with surrounding environments [53,54,77,79]. In the present study, since our aim is to explore the optical properties (e.g., absorption spectrum, EELS) of the examined vdW-HSs and the variation in them on moving from monolayer to heterobilayer, we therefore believe that without any loss of generality our study can account qualitatively well for the optical response of the vdW-HSs under consideration. The polarization of the electric field of the incident photon is also an important factor that plays a crucial role in determining the optical behavior of 2D materials [80]. We therefore calculate all the optical features and present the corresponding optical spectra along both x and z directions of polarization.

Figure 6 displays the real (ϵ_1) and imaginary (ϵ_2) part of the frequency-dependent dielectric constant of InSe/MoS$_2$, InSe/h-BN, and their constituent monolayers. The real part of dielectric function (ϵ_1) plays an important role in describing the optical properties of the material, where a transition of ϵ_1 from positive to negative value refers to the collective excitations of electrons. On analyzing our results, we find that for in-plane (out-of-plane) polarization it starts oscillating around the x-axis after 4.30 eV (5.43 eV) and 4.12 eV (2.58 eV) for InSe/MoS$_2$ and InSe/h-BN, respectively. Furthermore, the real part of the in-plane component of the dielectric function at zero energy, which is commonly called a static dielectric

constant, defines dielectric screening during the Coulomb interaction between the electrons and holes. For in-plane polarization, the static value at $\omega = 0$ is found to be 3.10, 5.78, and 1.52 eV for monolayer InSe, MoS_2, and h-BN, whereas 6.69 and 4.00 eV for InSe/MoS_2 and InSe/h-BN HSs, respectively. An increase in its value corresponds to lesser exciton binding energies, which suggests that electrons and holes can be easily dissociated in the examined heterobilayers as compared to their component monolayers.

The imaginary part of the dielectric constant helps in predicting the linear absorption properties of the material. In the case of in-plane polarization in monolayer MoS_2, a pronounced peak in the plot of ϵ_2 is found around 2.86 eV [see Fig. 6(c)] under consideration of the DFT + IPA scheme. This peak indicates the interband transition of electrons in monolayer MoS_2 and is in close agreement with the experimental value of 2.88 eV [81]. Concurrently, the most intense peak for the same optical feature is observed in between 3.60 and 4.01 eV for InSe and at 5.95 eV for h-BN monolayer, which also agrees well with previous theoretical and experimental results [70,78,82,83]. However, in the case of a heterobilayer of these materials, two intense peaks at 2.68 and 5.83 eV are found in the spectrum of InSe/MoS_2 [see Fig. 6(c)], while a broad dominant peak around 3.24–3.88 eV is found in the case of InSe/h-BN [see Fig. 6(g)]. This shows that in both of our vdW-HSs the first prominent peak is redshifted with respect to their component layers, and this shift is more prominent in the case of InSe/h-BN. For out-of-plane polarization, the ϵ_2 spectrum appears to be blueshifted as compared to in-plane polarization for all monolayers and their heterobilayers, except for the single-layer InSe, for which the spectrum is seen redshifted with the most intense peak at 2.98 eV [see Fig. 6(d)] [69]. Figure S5 of the Supplemental Material [32] reveals that the absorption coefficient for both of our vdW-HSs is in the order of 10^5 cm^{-1}, which is sufficient for good optical absorption required for solar cells. Interestingly, we also find that the absorption range of both of the examined HSs is a cumulative sum of their component layers, which is not only restricted in the visible light region, but is also distributed in the ultraviolet (UV) and near-infrared regions.

EELS has a particular importance in understanding the role of plasmons in metals and semiconductors. Due to the screening of an electric field by electrons, the light frequency above (below) the plasma frequency is transmitted (reflected) by materials. As a result, EELS can help in the characterization of materials. The theoretical EELS as obtained using DFT + IPA calculations for both the HSs is presented in Fig. 7, along with their component layers. In InSe monolayer along the x direction of polarization, we obtain two broad peaks at about 4.78–6.32 and 8.32–10.49 eV due to π and $\pi + \sigma$ electron plasmon, respectively [see Fig. 7(a)]. This result closely agrees with the experimental results of Politano *et al.* [82], who showed that EELS spectra of InSe accommodate a few distinct peaks at around 3.8, 6.0, and 9.0 eV, whereas along the z direction of polarization, multiple distinct peaks are noticed at 3.80, 5.76, 7.09, 8.56, and 9.82 eV under the DFT + IPA method [see Fig. 7(b)]. Similarly for in-plane polarization, resonant peak maxima for π and $\pi + \sigma$ electron plasmon are located at 8.04 (6.67) and 16.61 (16.79) eV in the case of MoS_2 (h-BN) monolayer, while these peaks
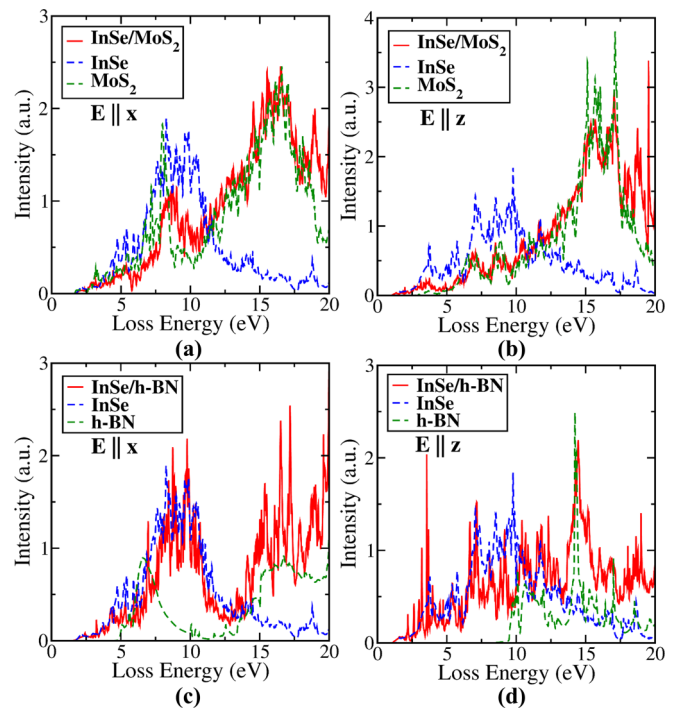
FIG. 7. The electron energy loss spectra (EELS) of (a) and (b) InSe/MoS_2 and (c) and (d) InSe/h-BN-based vdW-HSs, calculated using the DFT + IPA approach via the opt-PBE functional, along both x and z directions of polarization, respectively.

are seen redshifted (blueshifted) for out-of-plane polarization with maxima at 6.60 (10.14), 8.91 (14.30), and 17.17 (17.04) eV (see Fig. 7). This also agrees well with the previous reports [83–85].

The EELS of InSe/MoS_2 is, however, found to be quite distinct as compared to its constituent layers. It consists of a few prominent resonance features for in-plane-polarization at about 5.37, 8.77, and 16.54 eV [see Fig. 7(a)]. These peaks arise mainly due to collective π-π^* transitions within the InSe layer, π-σ^* and σ-π^* transitions within the intralayers, and σ-σ^* within the MoS_2 layer, respectively. Moreover, except for a redshift in the spectrum, the overall trend of the EELS spectrum for out-of-plane polarization has a similar regularity as compared to in-plane polarization [see Fig. 7(b)]. Interestingly, in InSe/h-BN, however, we noticed that due to the large band gap of h-BN, the EELS spectrum for in-plane polarization at low energy (i.e., below 12 eV) mainly follows the same trend of monolayer InSe. Thus, in DFT + IPA calculations, with a little redshift in the spectrum the lower energy peak at 4.36 eV for InSe/h-BN arises due to π-π^* transitions within the InSe layer, and another resonant peak at around 8.49–9.85 eV occurs due to π-σ^*, σ-π^*, and σ-σ^* transitions within the InSe layer [see Fig. 7(c)], whereas the energy loss above 15 eV is found to be dominated by the σ-σ^* transition within the h-BN layer. Similar to InSe/MoS_2, the EELS spectrum along the z direction of polarization for InSe/h-BN is also found to be redshifted [see Fig. 7(d)]. However, the obvious difference is in the range of 10–12.5 eV energy loss where the EELS spectrum features the $\pi + \sigma$

electron plasmon peak that originates due to intralayer electron transitions.

E. Elastic properties

The elastic behavior of 2D materials plays a vital role in their integration in practical devices. Therefore, to explore and understand the elastic properties of the examined heterobilayers from the perspective of their in-plane stiffness and bending flexibility, we calculated the layer modulus (γ), averaged Young's modulus (E), Poisson's ratio (v), and shear modulus (G) of the vdW-HSs using the following expressions [34]:

$$\gamma = \tfrac{1}{2}(C_{11} + C_{12}),$$

$$E = \frac{C_{11}^2 - C_{12}^2}{C_{11}},$$

$$G = C_{66},$$

and

$$v = C_{12}/C_{11}.$$

Furthermore, to see the variation in the mechanical properties on moving from monolayers to heterobilayers, we also calculated and tabulated the same parameters for the pristine monolayers (see Table I), which are found to be consistent with the available data in the literature [27,57–62]. Our calculations reveal that the elastic coefficients C_{11} and C_{66} of heterobilayers are higher than that of their constituent layers, while C_{12} is smaller as compared to the highest value of their component layers. This is not surprising and has been seen in various cases [57,59,65,86]. The values of C_{11} and C_{66} of a heterobilayer system are generally governed by the interlayer coupling coefficient of the HS, which in turn strongly depends on the van der Waals (vdW) interactions between the constituent layers and the interlayer friction coefficient [59]. Our calculations reveal the vdW energy of InSe/MoS$_2$ and InSe/h-BN HSs to be |0.635| and |0.384| eV/at, respectively. These values are comparable to the vdW energy of graphene/MoS$_2$ HS [57], which has also been found to show an improved elastic response as compared to the free-standing graphene and MoS$_2$ monolayer. On the other hand, a little decrease in the value of C_{12} in the heterobilayers as compared to the highest value of their component layers has also been witnessed in the case of black phosphorene/HfS$_3$ HS [65] and can primarily be attributed to the nonlinear elastic response of the constituent monolayers [57,60,87]. On analyzing the layer and Young's modulus of the HSs that represent the resistance of a nanosheet under stretching and the hardness of 2D materials, respectively, we found that the value of these parameters increases in InSe/MoS$_2$. This suggests that the examined HS is much stiffer than the InSe and MoS$_2$ monolayers. However, in the case of InSe/h-BN these physical parameters are found to be slightly lower than that of h-BN monolayers but much higher than InSe/MoS$_2$, suggesting they may be a potential candidate for practical large-magnitude strain engineering. Furthermore, an increase in the value of shear modulus is observed in the case of HSs,

which suggests that these HSs are superior charge transport materials compared with their component layers, since shear modulus defines the wrinkling and rippling behavior of 2D materials, which in turn control the scattering of charge carriers. Poisson's ratio, which characterizes the mechanical response of solid against external loads, is found to decrease from pristine monolayers to vdW-HSs. Since the monolayers are coupled with strong interlayer vdW interactions in the HSs, this is quite expected and can be seen in other work as well [88].

Another important parameter is the bending modulus, which defines the resistance against out-of-plane deformation of 2D materials such as wrinkles, ripples, and crumples under external strain. Within the continuum mechanics, therefore, we also studied the bending modulus (D) of the HSs as well as their constituent layers using the following equation [89]:

$$D = \frac{Yh^2}{12(1 - v^2)},$$

where h is the thickness of 2D materials. It is worthwhile to mention here that h varies with deformation strain, and an accurate measurement of h is uncertain through experiments. However, it is possible to determine the lower bound of the value with absolute thickness of the materials. Thus, for a qualitative analysis, we presume the thickness of InSe and MoS$_2$ with the Se-Se (d_{Se-Se}) and S-S (d_{S-S}) distance within the layer, respectively, while the thickness of h-BN is approximated with the thickness of a graphene layer (0.75 Å) [57]. Similarly, the thickness of HSs is determined by adding the interlayer distance with the thickness of constituents layers. A lower value of D (see Table I) suggests that h-BN can be bent easily as compared to InSe and MoS$_2$ monolayers. However, the combination yields a very large bending energy due to strong vdW interactions between the layers. This implies that the examined HSs can easily restrain the bending motion.

F. Carrier mobility

The transport properties of any material play a crucial role in deciding the performance of that material based optoelectronic devices. We therefore calculate the acoustic phonon-limited charge carrier mobility of InSe/MoS$_2$ and InSe/h-BN, along with their component layers in both the x and y directions of a lattice, by considering a standard 2D model discussed in the "Methods" section of the Supplemental Material [32]. The deformation constant, in-plane stiffness, and the charge carrier mobility of both the electron and the hole for the constituent and hybrid layers are tabulated in Table II, while details of the calculations are presented in Sec. 7 (see Figs. S6–S14) of the Supplemental Material [32]. On analyzing the results, we found that in agreement with previous reports [21,90] the carrier mobility of monolayer InSe is isotropic with the electron mobility ($\sim 10^3$ cm^2 V^{-1} s^{-1}) much higher than the hole mobility ($\sim 10^1$ cm^2 V^{-1} s^{-1}), whereas a completely opposite trend is seen for monolayer MoS$_2$, where hole mobility ($\sim 10^2$ cm^2 V^{-1} s^{-1}) dominates over electron mobility ($\sim 10^1$ cm^2 V^{-1} s^{-1}), which also agrees well with previous calculations [91]. In the case of monolayer h-BN, however, the hole mobility is found to be nearly isotropic and a little higher than the isotropic electron mobility with a value

TABLE II. The calculated carrier effective masses $m^*(m_0)$, deformation potential E_1 (eV), in-plane stiffness C_{2D} (eV/Å^2), and mobility μ (cm^2 V^{-1} s^{-1}) for electron (e) and hole (h) along the x and y directions in monolayer InSe, MoS$_2$, h-BN, as well as InSe/MoS$_2$ and InSe/h-BN vdW-HSs at room temperature (300 K). The effect of strain on the charge carrier mobility of InSe/MoS$_2$ and InSe/h-BN is also shown by considering $\sigma = \pm 4\%$ strain on the system.

Carrier	Strain	System	m_x^*	m_y^*	E_{1x}	E_{1y}	C_{2D-x}	C_{2D-y}	μ_x	μ_y	Reference
e	0%	InSe	0.20	0.21	−5.06	−5.05	3.46	3.46	1152.45	1099.31	This work
										1803–1995	Ref. [21] (Theory)
										1584–1667	Ref. [90] (Theory)
										10^3	Ref. [14] (Expt.)
	0%	MoS$_2$	0.74	0.54	−10.86	−10.86	9.64	9.64	59.88	82.14	This work
										60–72	Ref. [91] (Theory)
										30–60	Ref. [92] (Expt.)
										200	Ref. [93] (Expt.)
	0%	h-BN	0.95	0.96	−7.20	−7.20	20.16	20.16	147.14	145.52	This work
										487	Ref. [94] (Theory)
	−4%	InSe/MoS$_2$	0.22	0.22	−8.75	−8.51	16.72	16.41	1540.19	1600.31	This work
	0%	InSe/MoS$_2$	0.21	0.21	−5.94	−5.89	12.54	12.50	2749.77	2791.40	This work
	+4%	InSe/MoS$_2$	0.27	0.27	−4.45	−4.47	9.45	9.43	2238.57	2215.86	This work
	−4%	InSe/h-BN	0.19	0.19	−8.88	−8.12	11.17	12.74	1340.05	1829.61	This work
	0%	InSe/h-BN	0.18	0.18	−13.20	−12.98	23.45	23.44	1419.63	1468.00	This work
	+4%	InSe/h-BN	0.17	0.17	−12.31	−12.38	18.06	17.96	1408.96	1384.46	This work
h	0%	InSe	2.23	1.79	2.94	2.95	3.46	3.46	30.49	37.94	This work
										40	Ref. [20] (Expt.)
										94–127	Ref. [21] (Theory)
										143–152	Ref. [90] (Theory)
	0%	MoS$_2$	0.73	0.60	−5.58	−5.74	9.64	9.64	219.78	252.69	This work
										152–200	Ref. [91] (Theory)
										480	Ref. [92] (Expt.)
	0%	h-BN	0.38	0.62	−8.85	−8.85	20.16	20.16	482.14	295.51	This work
										500	Ref. [95] (Expt.)
	−4%	InSe/MoS$_2$	0.71	0.71	−5.32	−5.27	16.72	16.41	400.10	400.77	This work
	0%	InSe/MoS$_2$	1.40	1.31	1.23	1.30	12.54	12.50	1503.26	1433.34	This work
	+4%	InSe/MoS$_2$	0.76	0.81	0.28	0.35	9.45	9.43	67527.76	42108.42	This work
	−4%	InSe/h-BN	2.05	0.68	−1.79	−1.48	11.17	12.74	490.19	2483.28	This work
	0%	InSe/h-BN	1.89	2.01	−5.63	−5.66	23.45	23.44	68.58	63.69	This work
	+4%	InSe/h-BN	1.75	1.16	−5.95	−6.06	18.06	17.96	70.14	101.57	This work

of the order of 10^2 cm^2 V^{-1} s^{-1} (see Table II), in agreement with previous measurements [95].

Similar to monolayer InSe, the electron mobility of InSe/MoS$_2$ HS is also found to be isotropic, but its value is calculated nearly threefold [(2.7–2.8) × 10^3 cm^2 V^{-1} s^{-1}] higher than that of monolayer InSe (1.1 × 10^3 cm^2 V^{-1} s^{-1}). This slight increase in the value is attributed to the increase in the in-plane elastic stiffness (C_{2D}), which obviously would be higher for a few-layer structure due to strong vdW interactions. We found that the C_{2D} of InSe/MoS$_2$ vdW-HS is actually the sum of the same component layers (see Table II). Most interestingly, the hole mobility [∼(1.4–1.5) × 10^3 cm^2 V^{-1} s^{-1}] is also found to be of the same order as electron mobility, predicting the ambipolar charge transport characteristics for InSe/MoS$_2$. The high hole mobility is simply attributed to the modification of the CBM of the InSe layer due to strong interplane hybridization between Se-p_z and Mo-d_{z^2} orbitals in the presence of the MoS$_2$ layer, which decreases the hole effective mass (m^*) along the x and y directions, along with a significant decrease in the deformation potential constant (E_1) as well. For a similar reason,

the electron mobility [(1.4–1.5) × 10^3 cm^2 V^{-1} s^{-1}] is seen to increase in InSe/h-BN as compared to monolayer InSe. However, due to the large band gap of h-BN, the VBM of the InSe layer remains almost unmodified in the presence of the h-BN layer, and thus the hole mobility in InSe/h-BN is found to be comparable to the hole mobility of InSe monolayer.

The effect of in-plane mechanical strain on the carrier mobility InSe/MoS$_2$ and InSe/h-BN at room temperature is also investigated. It is found that in-plane compressive or tensile strain has a negligible effect on the electron effective mass. However, both the deformation potential E_1 and the in-plane elastic stiffness C_{2D} are found to modulate with external strain. They are found to increase (decrease) with compressive (tensile) strain in InSe/MoS$_2$, while they decrease in InSe/h-BN with both types of strain. However, these values compensate each other, resulting in the same order of electron mobility (10^3 cm^2 V^{-1} s^{-1}) in the strained structures. However, the hole mobility shows a contrasting behavior. In InSe/MoS$_2$ it gets enhanced by an order of magnitude with tensile strain and reaches a value of 6.7×10^4 and 4.2×10^4 cm^2 V^{-1} s^{-1} along the x and y directions,

respectively, while it decreases by an order of magnitude and attains a value of 4.0×10^2 cm^2 V^{-1} s^{-1} in both directions with compressive strain. On the contrary, the hole mobility is found to increase by an order of magnitude with compressive strain in InSe/h-BN [$(0.5–2.5) \times 10^3$ cm^2 V^{-1} s^{-1}], while it remains almost constant on the application of tensile strain [$(0.7–1.0) \times 10^2$ cm^2 V^{-1} s^{-1}]. Thus, our calculations predict that the hole mobility can be modulated to two orders of magnitude by applying variable strain to both vdW-HSs.

IV. CONCLUSIONS

We systematically investigated the stability as well as the electronic, optical, mechanical, and transport properties of InSe/MoS$_2$ and InSe/h-BN vdW-HSs using first-principles DFT-based calculations. The large negative binding energy and mechanical stability suggest that both of the examined vdW-HSs are stable and can be realized experimentally. Our calculations predict a moderate indirect band gap ($\sim$1.0 eV under the opt-PBE functional) for both of the HSs in their unperturbed ground state, and they also show that both the band gap and its nature can be largely tuned ($\sim$0.1–1.6 eV) by applying mechanical strain or/and a transverse electric field. At 4% compressive strain we noticed an indirect-to-direct transition in the band gap of InSe/MoS$_2$, where it exhibits type-II band alignment with a band gap of 1.49 eV (under the opt-PBE functional). Such materials can be extremely promising for photovoltaics, where it is possible to reduce the recombination rate through a spatial separation of electron and hole. Application of electric field between -0.1 and 0.1 V/Å is found to marginally affect the band gap by 0.02–0.06 eV, however a relatively larger variation

is observed beyond $E = \pm 0.1$ V/Å. The study of optical absorption spectra reveals that light absorption capability gets enhanced in heterobilayers as compared to their constituent monolayers. Similarly, the overall mechanical integrity is also seen to improve in the examined heterobilayers. Most importantly, InSe/MoS$_2$ is found to exhibit ambipolar charge carrier transport characteristics at room temperature with large electron [$(2.7–2.8) \times 10^3$ cm^2 V^{-1} s^{-1}] and hole [$(1.4–1.5) \times 10^3$ cm^2 V^{-1} s^{-1}] mobility. On the other hand, a slight increase in the electron mobility in InSe/h-BN [$(1.4–1.5) \times 10^3$ cm^2 V^{-1} s^{-1}] is predicted as compared to InSe monolayer (1.1×10^3 cm^2 V^{-1} s^{-1}). Interestingly, the induced in-plane strain is also found to significantly affect the charge carrier mobility. In particular, tensile (compressive) strain is found to dramatically increase the hole mobility for InSe/MoS$_2$ (InSe/h-BN) by roughly an order of magnitude at room temperature. In summary, this study elucidates that the bilayer heterostructures of InSe/MoS$_2$ and InSe/h-BN hold more promise than their constituent monolayers, with widely tunable optoelectronic and charge transport properties, which make them potential candidates for the next-generation optoelectronic devices in general, and photovoltaics in particular.

ACKNOWLEDGMENTS

[1] K. S. Novoselov, A. K. Geim, S. V. Morozov, D. Jiang, Y. Zhang, S. V. Dubonos, I. V. Grigorieva, and A. A. Firsov, Science **306**, 666 (2004).

[2] C. N. R. Rao, A. K. Sood, K. S. Subrahmanyam, and A. Govindaraj, Angew. Chem. **48**, 7752 (2009).

[3] M. J. Allen, V. C. Tung, and R. B. Kaner, Chem. Rev. **110**, 132 (2010).

[4] M. Coroş, F. Pogăcean, L. Măgeruşan, C. Socaci, and S. Pruneanu, Front. Mater. Sci. **13**, 23 (2019).

[5] J. D. Caldwell, I. Aharonovich, G. Cassabois, J. H. Edgar, B. Gil, and D. N. Basov, Nat. Rev. Mater. **4**, 552 (2019).

[6] W. Choi, N. Choudhary, G. H. Han, J. Park, D. Akinwande, and Y. H. Lee, Mater. Today **20**, 116 (2017).

[7] K. S. Thygesen, 2D Mater. **4**, 022004 (2017).

[8] W. Shockley and H. J. Queisser, J. Appl. Phys. **32**, 510 (1961).

[9] Z. Wang, Q. Li, Y. Chen, B. Cui, Y. Li, F. Besenbacher, and M. Dong, NPG Asia Mater. **10**, 703 (2018).

[10] C. Androulidakis, K. Zhang, M. Robertson, and S. Tawfick, 2D Mater. **5**, 032005 (2018).

[11] X. Wang, Y. Sun, and K. Liu, 2D Mater. **6**, 042001 (2019).

[12] V. Zólyomi, N. D. Drummond, and V. I. Fal'ko, Phys. Rev. B **89**, 205416 (2014).

[13] L. Debbichi, O. Eriksson, and S. Lebegue, J. Phys. Chem. Lett. **6**, 3098 (2015).

[14] D. A. Bandurin, A. V. Tyurnina, G. L. Yu, A. Mishchenko, V. Zólyomi, S. V. Morozov, R. K. Kumar, R. V. Gorbachev, Z. R. Kudrynskyi, and S. Pezzini *et al.*, Nat. Nanotechnol. **12**, 223 (2016).

[15] M. Brotons-Gisbert, D. Andres-Penares, J. Suh, F. Hidalgo, R. Abargues, P. J. Rodriguez-Canto, A. Segura, A. Cros, G. Tobias, and E. Canadell *et al.*, Nano Lett. **16**, 3221 (2016).

[16] D. V. Rybkovskiy, A. V. Osadchy, and E. D. Obraztsova, Phys. Rev. B **90**, 235302 (2014).

[17] L. Shi, Q. Zhou, Y. Zhao, Y. Ouyang, C. Ling, Q. Li, and J. Wang, J. Phys. Chem. Lett. **8**, 4368 (2017).

[18] A. A. Kistanov, Y. Cai, K. Zhou, S. V. Dmitriev, and Y. W. Zhang, J. Mater. Chem. C **6**, 518 (2018).

[19] S. Sucharitakul, N. J. Goble, U. R. Kumar, R. Sankar, Z. A. Bogorad, F. C. Chou, Y. T. Chen, and X. P. A. Gao, Nano Lett. **15**, 3815 (2015).

[20] D. Errandonea, D. Martínez-García, A. Segura, J. Ruiz-Fuertes, R. Lacomba-Perales, V. Fages, A. Chevy, L. Roa, and V. Munoz-San José, High Press. Res. **26**, 513 (2006).

[21] Y. M. Ding, J. J. Shi, C. Xia, M. Zhang, J. Du, P. Huang, M. Wu, H. Wang, Y. L. Cen, and S. H. Pan, Nanoscale **9**, 14682 (2017).

[22] D. Pierucci, H. Henck, J. Avila, A. Balan, C. H. Naylor, G. Patriarche, Y. J. Dappe, M. G. Silly, F. Sirotti, and A. T. C. Johnson *et al.*, Nano Lett. **16**, 4054 (2016).

[23] L. Yu, Y. H. Lee, X. Ling, E. J. G. Santos, Y. C. Shin, Y. Lin, M. Dubey, E. Kaxiras, J. Kong, and H. Wang *et al.*, Nano Lett. **14**, 3055 (2014).

[24] R. G. Parr and W. Yang, *Density-functional Theory of Atoms and Molecules* (Oxford University Press, Oxford, 1989).

[25] X. Chen, Z. Z. Lin, and M. Ju, Phys. Status Solidi RRL **12**, 1800102 (2018).

[26] J. Zhang, X. Y. Lang, Y. F. Zhu, and Q. Jiang, Phys. Chem. Chem. Phys. **20**, 17574 (2018).

[27] T. Hu, J. Zhou, and J. Dong, Phys. Chem. Chem. Phys. **19**, 21722 (2017).

[28] H. Shi, H. Pan, Y. W. Zhang, and B. I. Yakobson, Phys. Rev. B **87**, 155304 (2013).

[29] P. Johari and V. B. Shenoy, ACS Nano **6**, 5449 (2012).

[30] G. Kresse and J. Furthmuller, Phys. Rev. B **54**, 11169 (1996).

[31] G. Kresse and J. Furthmuller, Comput. Mater. Sci. **6**, 15 (1996).

[32] See Supplemental Material at http://link.aps.org/supplemental/10.1103/PhysRevB.101.235425 for methods, structural details, electronic structures of the component layers, electronic structures of the vdW-HSs, band alignments, optical properties, and details of charge carrier mobility.

[33] F. Birch, Phys. Rev. **71**, 809 (1947).

[34] R. C. Andrew, R. E. Mapasha, A. M. Ukpong, and N. Chetty, Phys. Rev. B **85**, 125428 (2012).

[35] H. Behera and G. Mukhopadhyay, International Conference on Physics of Emerging Functional Materials (PEFM-2010), *AIP Conference Proceedings No. 1313*, edited by D. K. Aswal and A. K. Debnath (AIP, New York, 2010), p. 152.

[36] I. G. Buda, C. Lane, B. Barbiellini, A. Ruzsinszky, J. Sun, and A. Bansil, Sci. Rep. **7**, 44766 (2017).

[37] H. L. Zhuang and R. G. Hennig, Chem. Mater. **25**, 3232 (2013).

[38] S. Ahmad and S. Mukherjee, Graphene **3**, 52 (2014).

[39] L. Liu, Y. P. Feng, and Z. X. Shen, Phys. Rev. B **68**, 104102 (2003).

[40] N. Berseneva, A. Gulans, A. V. Krasheninnikov, and R. M. Nieminen, Phys. Rev. B **87**, 035404 (2013).

[41] Y. Liu, N. O. Weiss, X. Duan, H. C. Cheng, Y. Huang, and X. Duan, Nat. Rev. Mater. **1**, 16042 (2016).

[42] D. Jariwala, T. J. Marks, and M. C. Hersam, Nat. Mater. **16**, 170 (2017).

[43] R. Cheng, F. Wang, L. Yin, Z. Wang, Y. Wen, T. A. Shifa, and J. He, Nat. Electron. **1**, 356 (2018).

[44] Z. Chen, J. Biscaras, and A. Shukla, 2D Mater. **4**, 025115 (2017).

[45] H. P. Komsa and A. V. Krasheninnikov, Phys. Rev. B **88**, 085318 (2013).

[46] J. Jalilian and M. Safari, Diamond Relat. Mater. **66**, 163 (2016).

[47] P. E. Blöchl, Phys. Rev. B **50**, 17953 (1994).

[48] G. Kresse and D. Joubert, Phys. Rev. B **59**, 1758 (1999).

[49] J. Klimes, D. R. Bowler, and A. Michaelides, J. Phys.: Condens. Matter **22**, 022201 (2010).

[50] J. Klimes, D. R. Bowler, and A. Michaelides, Phys. Rev. B **83**, 195131 (2011).

[51] J. Heyd, G. E. Scuseria, and M. Ernzerhof, J. Chem. Phys. **118**, 8207 (2003).

[52] S. Grimme, J. Antony, S. Ehrlich, and H. Krieg, J. Chem. Phys. **132**, 154104 (2010).

[53] J. Paier, M. Marsman, and G. Kresse, Phys. Rev. B **78**, 121201(R) (2008).

[54] M. Gajdos, K. Hummer, G. Kresse, J. Furthmüller, and F. Bechstedt, Phys. Rev. B **73**, 045112 (2006).

[55] J. Bardeen and W. Shockley, Phys. Rev. **80**, 72 (1950).

[56] J. Qiao, X. Kong, Z. X. Hu, F. Yang, and W. Ji, Nat. Commun. **5**, 4475 (2014).

[57] S. Singh, C. Espejo, and A. H. Romero, Phys. Rev. B **98**, 155309 (2018).

[58] J. W. Jiang, Z. Qi, H. Park, and T. Rabczuk, Nanotechnology **24**, 435705 (2013).

[59] K. Liu, Q. Yan, M. Chen, W. Fan, Y. Sun, J. Suh, D. Fu, S. Lee, J. Zhou, and S. Tongay *et al.*, Nano Lett. **14**, 5097 (2014).

[60] Q. Peng, W. Ji, and S. De, Comput. Mater. Sci. **56**, 11 (2012).

[61] J. Wu, B. Wang, Y. Wei, R. Yang, and M. Dresselhaus, Mater. Res. Lett. **1**, 200 (2013).

[62] A. Falin, Q. Cai, E. J. Santos, D. Scullion, D. Qian, R. Zhang, Z. Yang, S. Huang, K. Watanabe, and T. Taniguchi *et al.*, Nat. Commun. **8**, 15815 (2017).

[63] J. E. Padilha, R. H. Miwa, A. J. R. da Silva, and A. Fazzio, Phys. Rev. B **95**, 195143 (2017).

[64] R. Sen and P. Johari, ACS Appl. Mater. Interfaces **11**, 12733 (2019).

[65] B. Sa, J. Chen, X. Yang, H. Yang, J. Zheng, C. Xu, J. Li, B. Wu, and H. Zhan, ACS Omega **4**, 4101 (2019).

[66] K. F. Mak, C. Lee, J. Hone, J. Shan, and T. F. Heinz, Phys. Rev. Lett. **105**, 136805 (2010).

[67] A. Ramasubramaniam, Phys. Rev. B **86**, 115409 (2012).

[68] C. Elias, P. Valvin, T. Pelini, A. Summerfield, C. J. Mellor, T. S. Cheng, L. Eaves, C. T. Foxon, P. H. Beton, and S. V. Novikov *et al.*, Nat. Commun. **10**, 2639 (2019).

[69] M. Wu, J. J. Shi, M. Zhang, Y. M. Ding, H. Wang, Y. L. Cen, and J. Lu, Nanoscale **10**, 11441 (2018).

[70] F. Ferreira, A. J. Chaves, N. M. R. Peres, and R. Ribeiro, J. Opt. Soc. Am. B **36**, 674 (2019).

[71] C. Gong, H. Zhang, W. Wang, L. Colombo, R. M. Wallace, and K. Cho, Appl. Phys. Lett. **103**, 053513 (2013).

[72] S. K. Behera and P. Deb, RSC Adv. **7**, 31393 (2017).

[73] F. A. Rasmussen, P. S. Schmidt, K. T. Winther, and K. S. Thygesen, Phys. Rev. B **94**, 155406 (2016).

[74] Q. Peng and S. De, Phys. Chem. Chem. Phys. **15**, 19427 (2013).

[75] T. Li, Phys. Rev. B **85**, 235407 (2012).

[76] D. Q. Khoa, D. T. Nguyen, C. V. Nguyen, V. T. Vi, H. V. Phuc, L. T. Phuong, B. D. Hoi, and N. N. Hieu, Chem. Phys. **516**, 213 (2019).

[77] J. Yan, K. W. Jacobsen, and K. S. Thygesen, Phys. Rev. B **86**, 045208 (2012).

[78] J. Jalilian and M. Safari, Phys. Lett. A **381**, 1313 (2017).

[79] S. Sadki and L. Drissi, J. Phys.: Condens. Matter **30**, 255703 (2018).

[80] P. Johari and V. B. Shenoy, ACS Nano **5**, 7640 (2011).

[81] Y. Li, A. Chernikov, X. Zhang, A. Rigosi, H. M. Hill, A. M. van der Zande, D. A. Chenet, E. M. Shih, J. Hone, and T. F. Heinz, Phys. Rev. B **90**, 205422 (2014).

[82] A. Politano, D. Campi, M. Cattelan, I. B. Amara, S. Jaziri, A. Mazzotti, A. Barinov, B. Gurbulak, S. Duman, and S. Agnoli *et al.*, Sci. Rep. **7**, 3445 (2017).

[83] R. Beiranvand and S. Valedbagi, Optik **127**, 1553 (2016).

[84] A. Kumar and P. Ahluwalia, J. Phys. B **407**, 4627 (2012).

[85] F. Fossard, L. Sponza, L. Schué, C. Attaccalite, F. Ducastelle, J. Barjon, and A. Loiseau, Phys. Rev. B **96**, 115304 (2017).

[86] X. Li, Z. Wu, X. Zhu, G. Li, and C. Mi, Comput. Mater. Sci. **169**, 109134 (2019).

[87] R. C. Cooper, C. Lee, C. A. Marianetti, X. Wei, J. Hone, and J. W. Kysar, Phys. Rev. B **87**, 035423 (2013).

[88] H. Zhong, K. Huang, G. Yu, and S. Yuan, Phys. Rev. B **98**, 054104 (2018).

[89] J. W. Jiang, Front. Phys. **10**, 287 (2015).

[90] L. L. Yang, J. J. Shi, M. Zhang, Z. M. Wei, Y. M. Ding, M. Wu, Y. He, Y. L. Cen, W. H. Guo, and S. H. Pan, Chin. Phys. Lett. **36**, 097301 (2019).

[91] Y. Cai, G. Zhang, and Y. W. Zhang, J. Am. Chem. Soc. **136**, 6269 (2014).

[92] W. Bao, X. Cai, D. Kim, K. Sridhara, and M. S. Fuhrer, Appl. Phys. Lett. **102**, 042104 (2013).

[93] B. Radisavljevic, A. Radenovic, J. Brivio, V. Giacometti, and A. Kis, Nat. Nanotechnol. **6**, 147 (2011).

[94] S. Bruzzone and G. Fiori, Appl. Phys. Lett **99**, 222108 (2011).

[95] D. Litvinov, C. A. Taylor, and R. Clarke, Diamond Relat. Mater. **7**, 360 (1998).